Shape-Memory Transformations of NiTi: Minimum-Energy Pathways between Austenite, Martensites, and Kinetically Limited Intermediate States

N. A. Zarkevich and D. D. Johnson

Phys. Rev. Lett. **113**, 265701 — Published 24 December 2014

DOI: 10.1103/PhysRevLett.113.265701

Shape-memory transformations of NiTi: minimum-energy pathways between austenite, martensites, and kinetically-limited intermediate states

N. A. Zarkevich[1] and D. D. Johnson[1,2*]
[1] *The Ames Laboratory, U.S. Department of Energy, Ames, Iowa 50011-3020 USA; and*
[2] *Materials Science & Engineering, Iowa State University, Ames, Iowa 50011-2300 USA.*
(Dated: November 20, 2014)

NiTi is the most used shape-memory alloy, nonetheless, a lack of understanding remains regarding the associated structures and transitions, including their barriers. Using a generalized solid-state nudge elastic band (GSSNEB) method implemented via density-functional theory, we detail the structural transformations in NiTi relevant to shape memory: those between body-centered orthorhombic (BCO) groundstate and a newly identified stable austenite ("glassy" B2-like) structure, including energy barriers (hysteresis) and intermediate structures (observed as a kinetically limited R-phase), and between martensite variants (BCO orientations). All results are in good agreement with available experiment. We contrast the austenite results to those from the often-assumed, but unstable B2. These high- and low-temperature structures and structural transformations provide much needed atomic-scale detail for transitions responsible for NiTi shape-memory effects.

PACS numbers: 81.30.Kf, 81.05.Bx, 64.70.kd, 63.20.Ry

Nitinol [1], or NiTi near 50 at.% Ti, is the most used shape-memory alloy, recovering its original shape upon heating after a substantial mechanical deformation [2]. It finds applications in medical implants, industrial devices, thermally activated robotics at nano- and macro-scales, reading-glass frames, and brassieres – its most profitable use. In spite of such intensive use, the underlying physics and atomistic mechanics of the shape-memory effect in this "simple" binary alloy remain unclear. The solid-state transformation pathway governs the observed shape-memory behavior. While there have been many attempts to reveal the competing structures and key barriers, they relied on intuition but have not identified the actual path or structures. First and foremost, rather than a simple (but unstable) B2 structure always used heretofore, the stable high-temperature austenite phase was recently discovered to be a more complex structure [3], with configurations displaying prominent, correlated static displacements but remaining B2-like on average, acting similar to a phonon glass [4].

Here, using the GSSNEB method [5] implemented via density-functional theory (DFT), we consider the NiTi shape-memory transformations (without use of intuition) that involve all the relevant structures, see Fig. 1, i.e., the proposed groundstate base-centered orthorhombic (BCO) structure [6], newly discovered stable austenite structure [3], and observed B19' and R phases, along with the oft-used unstable B2. We identify the competing kinetically-limited structures along the pathway, e.g., the observed R-phase [7], and the relevant transition states, including those among BCO variants responsible for the deformations of martensite. Our calculated small austenite-to-martensite energy barrier compares well with the observed narrow hysteresis [8]. (Hysteresis width increases monotonically with barrier [9, 10].) The path, structures, and transition states provide the first complete view of the NiTi shape-memory transformation, essential for processing and design.

To understand NiTi shape-memory transformations, structures of endpoint martensites and austenite are required. The groundstate is accepted as BCO [3, 6, 11]. The smallest stable austenite structure has a hexagonal ($Ni_{27}Ti_{27}$) cell [3], Fig. 2d, and DFT results agree well with all available calorimetry, x-ray diffraction (structure) and neutron diffraction (phonon density of states) data [3]. Multiple attempts have been made to visualize via atomic-scale simulations the NiTi austenite-to-martensite transformation (Fig. 1), all with B2-austenite assumed. Molecular dynamics [12, 13] based on a semi-

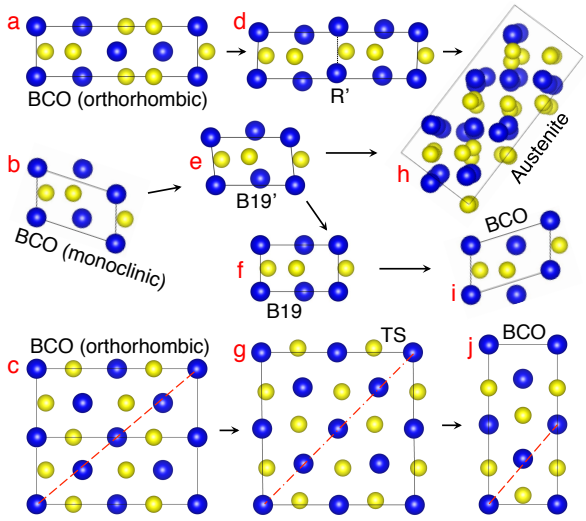

FIG. 1: (color online) Relevant structures [Ni (smaller, yellow) and Ti (larger, blue)] in $[010]_{BCO}$ (a, b, d, e, f, h, i) and $[001]_{BCO}$ (c, g, j) projections. BCO (a, b, c, i, j), Austenite (h), and intermediates: R' (d) and B19' (e). Shown also are BCO-to-BCO transition states: B19 (f) and twin (g).

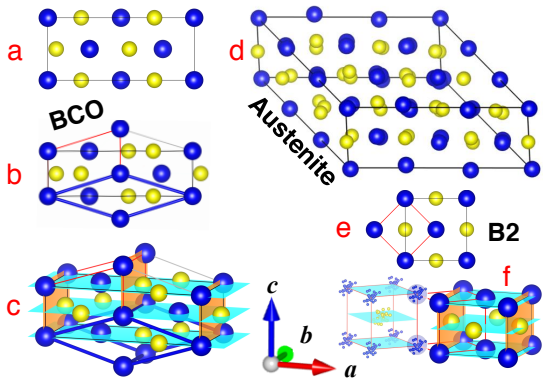

FIG. 2: (color online) (a) [001] and (b) [010] projections of (c) BCO; (d) stable austenite (Fig. 1h, represented by 54-atom hex cell [3]), compared to (e) [001] projection of (f) unstable B2 (compared to austenite displacements projected onto B2).

empirical potentials yielded two major stress-induced transformation from B2(austenite)-to-B19'(martensite), missing the observed BCO groundstate with B19' lower than BCO by 8 *me*V/NiTi [13]. Shear-shuffle models of detwinning were considered using DFT [14–17], some guided by intuition, yet there has been no success in modeling the austenite-to-BCO martensitic transformation. For a hypothetical two-step B2–B19–B19' pathway [17], a B2–B19 transition state was 13 *me*V/NiTi above B2. However, GSSNEB finds that the B2–BCO transformation bypasses B19 and has no barrier (reflecting the instability of B2), in agreement with experiment [18]. Hence, in spite of the considerable attention attracted by shape-memory Ni-Ti, the atomic-scale understanding of its shape memory remains incomplete.

Methods: For DFT method, we utilize VASP [19, 20] in a generalized gradient approximation (GGA) [21, 22] and projected augmented wave (PAW) basis [23]. We used a 337.0 *e*V planewave energy cutoff and 544.6 *e*V augmentation charge cutoff. Converged k-meshes have at least 50 k-points per Å^{-1} (e.g., $11 \times 13 \times 17$ for a $4.92 \times 4.00 \times 2.92$ Å cell). A modified Broyden method [24] is used for convergence. GSSNEB calculations are completed using Gaussian smearing (0.05 *e*V), and the tetrahedron method with Blöchl corrections verify the energies relative to BCO. Two representative structures of austenite – hexagonal unit cells of 54- and 108-atom (i.e., doubled along a) – were obtained by *ab initio* molecular dynamics followed by atomic relaxations at 0 K using the conjugate gradient method [3].

Transition states (TS) are obtained via the GSSNEB method [5] modified to use two climbing images [25], providing for complex potential-energy landscapes a more reliable minimum-energy path (MEP) $E(\{R_i^\lambda\},\lambda)$, with atoms at $\{R_i^\lambda\}$ along reaction path λ. Generally, the gradient $\nabla_\lambda E$ is the driving force for the structural transformation [5]. The kinetically-limited states (ones with a small driving force) can be made metastable by anisotropic stress. Indeed, a stationary R-phase stabilized by coherent stress is observed near off-stoichiometric precipitates [26], while a stress-induced R-phase is detected during the formation of martensite [7, 27].

The MEP $E(\lambda)$ provides details of the solid-solid transformation, including the transition probability p. Considering the TS – austenite free energy difference $\Delta F = \Delta E - T\Delta S$ with the energy (entropy) difference ΔE (ΔS), $p = e^{-\Delta F/k_BT} = e^{\Delta S/k_B} e^{-\Delta E/k_BT}$. Notably, however, only vibrations contribute to entropy (there is no chemical disorder). The TS is near austenite along λ (Fig. 4), so $|\Delta S|$ is small compared to the maximum (austenite–BCO) entropy difference $\Delta S_{max} = 0.33\, k_B$/atom at 333 K, where the transition is observed. We calculated ΔS_{max} from the phonon density of states [3], whose value is rather insensitive to temperature. Hence, for $\Delta S/k_B \to 0$, $e^{\Delta S/k_B} \approx 1$, and $p \approx e^{-\Delta E/k_BT}$. Thus, the MEP determines the energy barriers and transition probabilities, relevant to hysteresis.

STRUCTURES AND DEFORMATIONS

Ground State: BCO structure is the DFT groundstate [3, 6, 11]. Our calculated lattice constants are 2.9217, 4.0024, and 4.9189 Å, with an angle of 107.23°, defined in the monoclinic unit cell (Fig. 1b). BCO consists of two interpenetrating hcp sublattices, populated by Ni and Ti, respectively, with slightly displaced atoms due to Ni–Ti interaction (Fig. 2 a, b, c).

Deformed Martensite: Monoclinic B19' ($\vartheta \approx 98°$) is a low-energy deformation of BCO (Fig. 1e), as observed [28]. With BCO viewed as B19' with $\vartheta \approx 107°$, the energy of B19' is from 0 to 16 *me*V/atom higher than BCO, see Figs. 3 and 4 (agreeing with Fig. 1a in [6]). In the martensite, the experimental B19' structure is not the ground state, but its low-energy deformation, stabilized by the martensitic stress, and the ease to deform martensite accounts for its "superelasticity". Perfect BCO can be represented by B19' unit cells of two alternating or same orientations, giving boundaries between them that cost no energy (Fig. 2); it also produces low-energy twins.

Deformation Twins: Deformation of martensite is accompanied by motion of twins and other planar defects. Motion of twins was recently addressed in B19' and B2 structures [14, 15]. While pseudo-twinning in B2 NiTi has been suggested as impossible [29], perfect B2 is unstable and its structure is not relevant to the martensitic transformation. Approximated by periodic twins separated by 12.2 Å, DFT energy for (210)-twins in BCO is extremely low at 0.53 *me*V/Å^2 (or 8.4 *m*J/m^2); when separated by only 6 Å, the twin energy of 0.83 *me*V/Å^2 (or 13.3 *m*J/m^2) is higher, so twins repel at small distances, in agreement with observation [7].

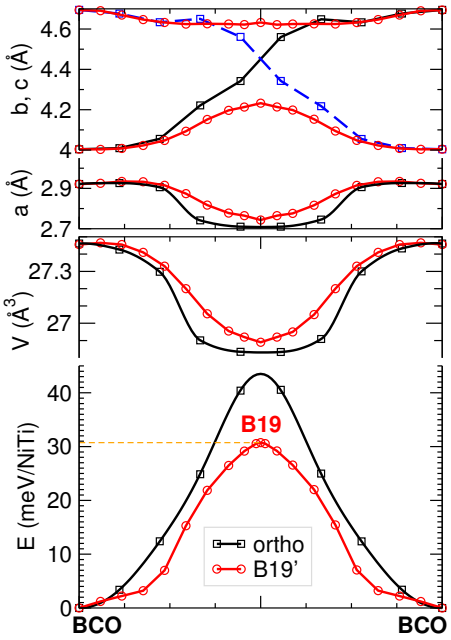

FIG. 3: (color online) GSSNEB MEP of BCO-to-BCO. Orthorhombic distortion (squares) interchanges the lattice constants b (solid black) and c (dashed blue line) . Shear of the monoclinic B19' cell (red circles) has B19 transition state; $c \cdot \sin\theta$ is plotted as the lattice constant normal to a and b.

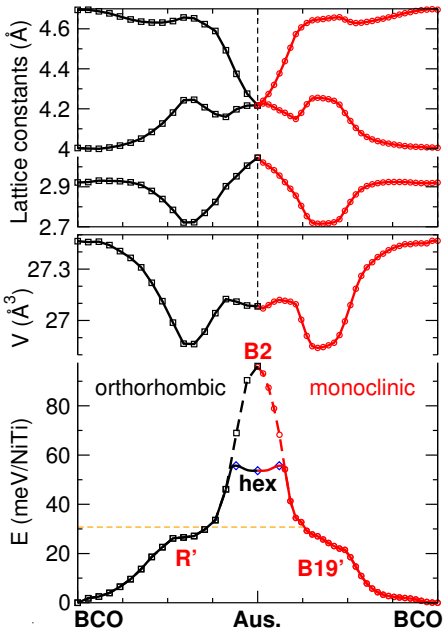

FIG. 4: (color online) GSSNEB MEP from BCO to austenite (solid line) and to unstable B2 (dashed) in orthorhombic (left, black) and monoclinic B19' (right, red) unit cells. B19 energy from Fig. 3 is given by the horizontal (orange) dashed line.

Austenite: The stable austenite structure, with representative $Ni_{27}Ti_{27}$ hexagonal cell, has a DFT energy of $E = 29.5$ meV/atom above BCO [3], giving an estimated [30] martensitic temperature $T_c \approx E/k_B = 343$ K, near the observed [31] 333 K for stoichiometric NiTi. A larger structure for austenite-to-BCO MEP calculations is constructed from the 54-atom cell in Fig. 2(d) by doubling along a. The resulting $Ni_{54}Ti_{54}$ structure (without 3 Å periodicity along a) has the same energy and similar displacements and properties as $Ni_{27}Ti_{27}$ austenite [3], so it too can be used to model austenite. This newly reported austenite looks B2-like "on average" (Fig. 2f), i.e., if atomic positions are averaged into a 2-atom B2 cell [3].

For completeness, the Ni-Ti phase diagrams [32, 33] reference the cubic B2 (Fig. 2 e, f) as the high-temperature solid phase. Our DFT B2 lattice constant is 3.0028 Å, in agreement with previous calculations [3, 6, 11]. Powder diffraction measurements [18, 34, 35] give 3.015 Å at 353 K. Our DFT energy for B2 is 48 meV/atom above BCO, agreeing with previous calculations [3, 6, 11], and corresponds to an estimated martensitic temperature of 557 K, well above that observed [31]. Importantly, B2 is known to be unstable, with imaginary phonon modes not stabilized by entropy below melting [3, 18]. We find no barrier for a B2-to-BCO transition (Fig. 4), confirming the B2 instability.

MEP AND TRANSITION STATES

BCO-to-BCO: First, we examine the solid-solid transformations between various orientations of BCO (Fig. 3). We find several transition states, with the lowest-energy B19 being only 15.4 meV/atom above BCO, similar in structure and energy to the kinetically limited R-phase (Fig. 1). Among the two TS in Fig. 1 (f, g), the more symmetric Ni_8Ti_8 TS (g) with the orthogonal lattice vectors $a = b \neq c$ (a=b=8.9, c=2.7 Å) is expected to be higher in energy compared to B19 Ni_2Ti_2 with $a \neq b \neq c$ (a=4.62, b=4.21, c=2.76 Å). Interestingly, the lowest-energy B19 TS (Fig. 1f) and the kinetically–limited intermediate structures in Fig. 1d,e have similar local atomic structure and comparable energies (horizontal dashed line in Figs. 3 and 4).

Austenite-to-Martensite: This transition occurs between the low-T B19'/BCO martensite and high-T austenite, represented by our stable $Ni_{27}Ti_{27}$ or $Ni_{54}Ti_{54}$ cells. $Ni_{27}Ti_{27}$ doubled along a (Fig. 2d) transforms into BCO structure if tripled along a (Fig. 2a), as shown for the orthorhombic path in Fig. 1 (a-d-h). The MEP from the austenite-to-BCO has a barrier of only 1 meV/atom above the austenite (Fig. 4). However, we also find other pathways with energy barriers above the austenite from 1 to 3.5 meV/atom; such barriers can be strongly affected by non-hydrostatic stress. The hysteresis width monotonically increases with the barrier height, starting from no hysteresis for zero barrier. A small barrier of

only 1 *me*V/atom agrees with a narrow hysteresis (within 40 K) in experiment [8].

We find that this transformation proceeds through multiple, kinetically–limited intermediate states, characterized by higher density and reduced unit-cell volumes, observed in experiment as an R-phase [36–38]. These intermediate states appear along the MEP in the regions labeled R' and B19' in Fig. 4 and have similar DFT energies (13.2 *me*V/atom above BCO), lattice constants and densities. Because the energy gradient $\nabla_\lambda E$ versus MEP (reaction) coordinate λ is the driving force, equilibrating this force by anisotropic stress makes them metastable. States with the smallest $|\nabla_\lambda E|$ can be stabilized by a moderate anisotropic stress, and such R-phase structures are indeed found [26, 27] near precipitates and during the martensitic transformation. Different transformation paths contain similar (but not identical) kinetically-limited states (Fig. 1 d, e) with local atomic arrangements like a B19 TS in Fig. 1f. We emphasize that mechanical deformation of martensite and its transformation to austenite upon heating proceed through similar intermediate structures.

Of course, the martensitic transformation happens without diffusion, only by local atomic rearrangements. The *ideal* local atomic positions are "remembered" in spite of displacements of atoms (relative to unstable B2 positions) in austenite. Austenite has substantial atomic displacive disorder at any temperature (not a classical thermal disorder of a perfectly ordered crystal), but displacements from ideal B2 do not exceed 1/4 of the B2 nearest-neighbor distances. Transformations between these two phases, namely, an easily deformable "superelastic" martensite and austenite with arrangement of displacively disordered but "leashed" atoms, account for the interesting shape-memory effect observed in NiTi alloys.

In summary, we addressed the structures and transformation relevant to NiTi shape-memory behavior, both austenite-to-martensite and martensite-to-martensite. These transformations include a newly identified austenitic structure, intermediate states (related to an R-phase), and low-energy deformations of BCO (observed as B19'), as well as the BCO groundstate. We also included the (unstable) B2 structure – historically (but incorrectly) assumed as the austenite phase in shape-memory studies.

Together the martensites, austenite, transitional and intermediate states, with their specific atomic displacements and structural deformations, provide the first atomic-scale understanding of the transformations responsible for the NiTi shape-memory effects. Our results agree with the observed B19' martensitic structure and its super-elasticity. The multiple low-energy planar defects, including twins, within BCO (needed to form a martensite) agree with the experimental observations [7]. Considering the austenite-to-martensite transformations, we found multiple pathways proceeding through kinetically–limited states, which are similar to the lowest-energy B19 transition state (B19' intermediate states) for the BCO-to-BCO transform. Although such intermediate states differ in atomic structure, all of them are similar in energy and density, which agrees with the measured increased density in the R-phase, and the variety of the R-phase structures suggested from experiments.

Acknowledgments: This work was supported by the U.S. Department of Energy (DOE), Office of Science, Basic Energy Sciences, Materials Science and Engineering Division. The research was performed at the Ames Laboratory, which is operated for the U.S. DOE by Iowa State University under contract DE-AC02-07CH11358.

* Electronic address: zarkev@ameslab.gov,ddj@ameslab.gov

[1] W. J. Buehler, J. W. Gilfrich, and R. C. Wiley, J. Appl. Phys. **34**, 475 (1963).
[2] V.G. Pushin, S.D. Prokoshin, R.Z. Valiev, V. Brailovski et al., *Titanium nickelide shape memory alloys* (UrB RAS, 2006).
[3] N. A. Zarkevich and D. D. Johnson, Phys. Rev. B **90**, 060102R (2014).
[4] T. Takabatake, K. Suekuni, T. Nakayama, and E. Kaneshita, Rev. Mod. Phys. **86**, 669 (2014).
[5] D. Sheppard, P. H. Xiao, W. Chemelewski, D. D. Johnson, and G. Henkelman, J. Chem. Phys. **136**, 074103 (2012).
[6] X. Y. Huang, G. J. Ackland, and K. M. Rabe, Nat. Mater. **2**, 307 (2003).
[7] K. Otsuka and X. Ren, Progress in Materials Science **50**, 511 (2005), ISSN 0079-6425.
[8] R.F. Hamilton, H. Sehitoglu, Y. Chumlyakov, H.J. Maier, Acta Mater. **52**, 3383 (2004).
[9] Z. Zhang, R. D. James, and S. Müller, Acta Mater. **57**, 4332 (2009), ISSN 1359-6454.
[10] J. Cui et al., Nature Mater. **5**, 286 (2006).
[11] K. Guda Vishnu and A. Strachan, Acta Mater. **58**, 745 (2010), Phys. Rev. B **85**, 014114 (2012).
[12] K. Saitoh, T. Sato, and N. Shinke, Mater. Trans. **47**, 742 (2006).
[13] Y. Zhong, K. Gall, and T. Zhu, J. Appl. Phys. **110**, 033532 (2011), Acta Mater. **60**, 6301 (2012).
[14] T. Ezaz, H. Sehitoglu, and H. J. Maier, Acta Mater. **59**, 5893 (2011), ibid **60**, 339 (2012).
[15] T. Ezaz and H. Sehitoglu, Appl. Phys. Lett. **98**, 141906 and 241906 (2011).
[16] T. Ezaz, J. Wang, H. Sehitoglu, and H. J. Maier, Acta Mater. **61**, 67 (2013).
[17] S. Kibey, H. Sehitoglu, and D. D. Johnson, Acta Mater. **57**, 1624 (2009).
[18] F. E. Wang, W. J. Buehler, and S. J. Pickart, J. Appl. Phys. **36**, 3232 (1965).
[19] G. Kresse and J. Furthmüller, Comput. Mat. Sci. **6**, 15 (1996).
[20] G. Kresse and J. Furthmüller, Phys. Rev. B **54**, 11169 (1996).
[21] J. P. Perdew, Phys. Lett. A **165**, 79 (1992).

[22] J.P. Perdew, J.A. Chevary, S.H. Vosko, K.A. Jackson, M.R. Pederson, D.J. Singh, and C. Fiolhais, Phys. Rev. B **46**, 6671 (1992), ibid **48**, 4978 (1993).
[23] P.E. Blöchl, Phys. Rev. B **50**, 17953 (1994).
[24] D.D. Johnson, Phys. Rev. B **38**, 12807 (1988).
[25] N. A. Zarkevich and D. D. Johnson (2014), submitted.
[26] M. Kurumada, Y. Kimura, H. Suzuki, O. Kido, Y. Saito, and C. Kaito, Scripta Mater. **50**, 1413 (2004), ISSN 1359-6462.
[27] J. Olbricht, A. Yawny, J. L. Pelegrina, G. Eggeler, and V.A. Yardley, J. Alloys Compd. **579**, 249 (2013).
[28] I. I. Sasovskaya, S. A. Shabalovskaya, and A. I. Lotkov, Zh. Eksp. Teor. Fiz. **77**, 2341 (1979).
[29] A. T. Paxton, Acta Metall. Mater. **43**, 2133 (1995).
[30] N. A. Zarkevich, T. L. Tan, and D. D. Johnson, Phys. Rev. B **75**, 104203 (2007).
[31] R. J. Wasilewski, S. R. Butler, J. E. Hanlon, and D. Worden, Metall Trans. **2**, 229 (1971).
[32] B. M. Danilenko, G. M. Lukashenko, and S. B. Prima, Sov. Powder Metall. Met. Ceram. **30**, 412 (1991), translated from: Poroshkovaya Metallurgiya 5, 73–75 (1991).
[33] P. Bellen, K. C. H. Kumar, and P. Wollants, Z. Metallkd. **87**, 972 (1996).
[34] R. Schmidt, M. Schleretht, H. Wipf, W. Assmus, and M. Müllner, J. Phys.: Condens. Matter **1**, 2473 (1989).
[35] R. Schmidt, M. Schlereth, H. Wipf, W. Assmus, and M. Müllner, Z. Phys. Chem. Neue Fol. **164**, 803 (1989).
[36] P. Sedlak, M. Frost, B. Benesova, T. Ben Zineb, and P. Sittner, Int. J. Plasticity **39**, 132 (2012).
[37] P. Sittner, P. Sedlak, M. Landa, V. Novak, and P. Lukas, Mat. Sci. Eng. A - Struct. **438**, 579 (2006).
[38] J. Uchil, K. K. Mahesh, and K. G. Kumara, Physica B **324**, 419 (2002).